Journal of Alloys and Compounds 695 (2017) 2190–2198

Contents lists available at ScienceDirect

Journal of Alloys and Compounds

journal homepage: http://www.elsevier.com/locate/jalcom

Design and operation of a hydrogen purification prototype based on metallic hydrides

E.M. Borzone [a, *], A. Baruj [a, b], G.O. Meyer [a, b]

[a] Instituto Balseiro and Centro Atómico Bariloche, CNEA-U.N. Cuyo, Argentina
[b] CONICET, Argentina

ARTICLE INFO

Article history:
Received 13 September 2016
Received in revised form
28 October 2016
Accepted 5 November 2016
Available online 8 November 2016

Keywords:
Hydrogen purification
Hydrogen recovery
Metal hydride
AB5
Mathematical modeling
Gas-solid reaction

ABSTRACT

A hydrogen purification device has been designed and implemented at a prototype scale. The device operation is based on the use of a hydride forming material distributed in two reaction beds, which work in opposition. Under the proposed design, one of the reactors receives the incoming gas, absorbing the hydrogen in it, while the other one desorbs pure hydrogen after a brief venting stage in which contaminants are eliminated. Thus, a continuous flow is processed. The reactors are thermally coupled in order to use the heat of reaction and save energy, working at room temperature without the need of additional heat sources or sinks.

The reaction's behavior can be described by a lumped computational model. The model is validated against measured results with pure H_2 at different flow rates. This computational tool is used to analyze the system behavior, in terms of hydrogen recovery fraction, under different working conditions, including the presence of trace amounts of CO in the feed gas. Purification experiments are performed using humidified hydrogen where the water vapor content is measured online. As an example scenario, using 300 g of $LaNi_5$ and a gas flow rate of 100 standard cm^3/min, the process successfully lowers the humidity content in the gas from 3000 ppmv to 190 ppmv, while achieving a hydrogen recovery fraction of 95%.

1. Introduction

Standard hydrogen purification methods like Pressure Swing Adsorption (PSA) are economically viable only under large hydrogen flow scenarios. This kind of scenario is not usual in small to medium sized industrial facilities. The initial investment needed to implement PSA can be prohibitively high for that type of company. Thus, there is an opportunity for developing hydrogen purification systems oriented to applications in these scales. Specifically, systems based on the use of metal hydrides have shown to be a versatile alternative in these scenarios, with a lower initial capital cost and less operating and maintenance requirements [1–3].

The potential of hydride forming materials (HFMs) as hydrogen purifying media has been already recognized and mentioned during the early developing of these materials [4]. However, there are only a few concrete examples of HFMs used in prototypes or in real life purification applications. Sheridan et al. presented in 1983 a paper describing a hydride-based hydrogen purifier that used $LaNi_5$ embedded in an inert metal particle bed. A pilot-plant scale system was built and tested, which was able to recover up to 94% hydrogen although its purity was not very high mainly due to the difficulty of quickly removing contaminants from the metal bed [4]. Later on, in 1987, Block et al. presented a design of a hydrogen purifier/compressor which included a 4-reactor design [5]. In order to prevent the selected HFM ($MmNi_{4.5}Al_{0.5}$) from poisoning, the design included a pre-purification system. The system was able to reach high purification levels, although the high outlet pressure requirement (100 bar) imposed several specific design tradeoffs. The first successful in-situ hydride-based hydrogen purification application was reported by Au et al. in 1996 [6]. They installed a 4-tanks hydrogen purifier containing 1600 kg of an undisclosed AB_5 alloy ($MmNi_{5-x}Al_x$) in a float glass production plant. The device was successfully used to separate hydrogen from a gas mixture that included Ar, N_2 and CH_4, while NH_4, CO and H_2O where previously removed from the gas flow by standard methods. The system was

* Corresponding author. Centro Atómico Bariloche, Av. Bustillo 9500, 8400 S. C. de Bariloche, Argentina.
E-mail address: emiliano.borzone@cab.cnea.gov.ar (E.M. Borzone).

http://dx.doi.org/10.1016/j.jallcom.2016.11.067
0925-8388/

able to reach a hydrogen recovery ratio of 70% (50 Nm^3/h) while the recovered hydrogen had a 99.999% purity, which was high enough to be reused in the production process. Recently, Miura et al. introduced a HFM-based hydrogen purifying system oriented at the final conditioning stage of a reformed gas that would be fed to a PEM fuel cell [7]. In this case, CO and H_2O were initially removed from the gas flow and the hydride-based device using $MmNi_{3.99-}Co_{0.6}Mn_{0.36}Al_{0.05}$ was able to recover up to 83% of hydrogen. The system used water at 20 °C and 80 °C as heat reservoirs to compensate thermal changes during hydrogen absorption and desorption, respectively.

These previous investigations and developments have some elements in common. One of them is the use of pre-purifying stages in order to remove from the gas flow those species considered detrimental to the performance of the hydride bed. In particular, most systems had in place standard CO and H_2O removal units. Only recently, the possibility of using surface-modified HFMs was successfully tested in a hydrogen purification scheme [8]. Another important limitation arises when considering the use of HFM-based purifiers under continuous process scenarios. In principle, a hydride bed can be either absorbing or desorbing hydrogen and, therefore, it could not be used to purify a steady hydrogen flow. This limitation has been circumvented by designing systems that included several hydride tanks [5,6,8]. While this kind of solution allows working in a continuous manner, the heat involved in the reactions must either be provided or dissipated by external means, thus increasing the system energy and water consumption. In an early attempt to solve this problem, an inert metal ballast was included in the reactor bed [4]. In this way, the temperature variations were reduced but the system showed low purity levels. This problem was attributed to the contaminants occluded between the metal pellets that could not leave the reactor during the venting stage. They were only removed by sweeping with the recovered hydrogen flow.

A different approach was recently proposed by Talagañis et al. that consists in thermally coupling two reactors in order to effectively use the heat flow generated during the hydriding stage in one reactor to favor the dehydriding process in the other one [9]. In this way, no heating and/or cooling systems would be required and the only energy cost would be linked to the hydrogen pressure loss in the device. This work presents the design, construction and testing of an in-line hydrogen purification prototype based on this approach. The work is part of a study to assess the convenience of recovering hydrogen gas from a metal products manufacturing plant. The plant currently uses a 24 Nm^3/h flow of hydrogen in a surface reduction process during which small amounts of impurities are incorporated to the gas stream. The main contaminant under the plant conditions is H_2O, which is continuously monitored by means of a dew point sensor. The exhaust gas typically contained up to 1000 ppm of H_2O, apart from minor contents of other contaminants such as CO_2, CO and CH_4. As previous works in hydrogen purification methods based on HFMs always included a water separation stage when H_2O was present, one of the objectives of this paper is to determine whether a hydride-based system can accomplish purification under this scenario without an additional drying stage.

2. Experimental details

2.1. Layout

The designed purification device has two reactors (R_1 and R_2 in Fig. 1). These are thermally coupled and are sought to work in opposition. Therefore, while one reactor is in the hydrogen absorption stage, the other one is either venting impurities or desorbing purified hydrogen. The piping schema of the device is also shown in Fig. 1. Inlet and outlet gas flows are regulated by mass flow controllers F_i and F_o, respectively. Venting is performed through a mechanical vacuum pump. The solenoid valves v_1 to v_6 allow the connection of either reactor to the inlet or outlet lines, as well as to the venting line. Pressure (P_1, P_2) and temperature (T_1, T_2) in each reactor are continuously monitored, as well as the room temperature (T_{room}). The water vapor content in the gas flow is measured at the inlet pipe to one of the reactors by means of a dew-point sensor (denoted as H_2O in Fig. 1). The placement of this dew-point sensor is such that it allows measuring the water vapor content of the gas flow during all stages (absorption, venting, desorption). Control and data acquisition functions are implemented by software developed at our laboratory, which allows for the flexible design of different experimental procedures.

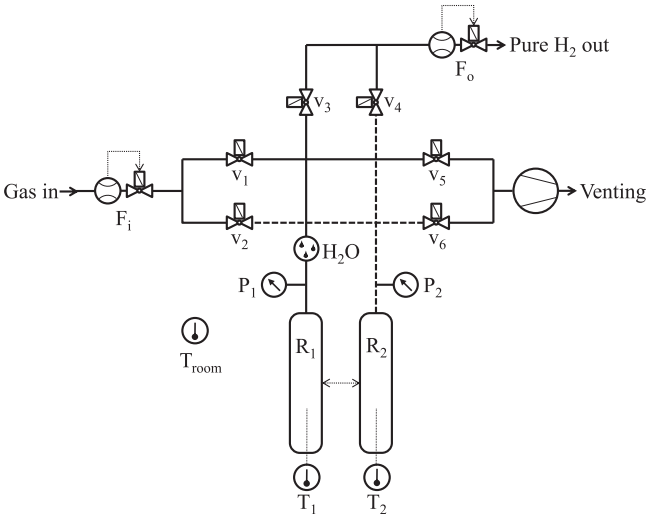

Fig. 1. Piping layout of the device. R_1 and R_2 are the thermally coupled reactors, P_1 and P_2 pressure sensors, T_1, T_2 and T_{room} temperature sensors, H_2O a humidity sensor, F_i and F_o mass flow controllers and v_1 … v_6 solenoid valves.

The operation sequence is as follows. Both reactors and all internal volumes are evacuated at the initial condition. All valves are initially closed. The process starts by setting the inlet gas flow (F_i) and opening valve v_1 to initiate hydrogen absorption in reactor R_1. This condition is kept until the reactor pressure reaches a preset value, P_{max}. Then valve v_1 is closed and valve v_2 opened, initiating the absorption cycle of reactor R_2. Meanwhile, valve v_5 is briefly opened in order to vent the gases present in R_1. Once the venting stage is completed, v_5 is closed and valve v_3 is opened to allow the purified hydrogen desorption from R_1. This purified flow is set at a constant value by means of the outlet mass-flow controller (F_0). The system remains under this condition until P_2 reaches P_{max}, thus ending the absorption stage at R_2. At this point, v_2 and v_3 are closed, R_2 is briefly vented via v_6 and subsequently desorbed by opening v_4, while v_1 is opened again in order to re-initiate the absorption stage in R_1. By a cyclic repetition of this procedure a continuous operation is achieved where the inlet flow is uniform and the outlet flow is briefly interrupted during venting stages.

For the case of water vapor removal experiments, the feed hydrogen flow was humidified in-line, immediately before entering the device. This was accomplished by directing the flow through a vertically placed 500 cm^3 cylinder, half-filled with distilled water. The dew-point obtained during tests by this procedure consistently showed values around 12 °C.

2.2. Reactor design

A review of commonly used reactor designs for HFMs can be found in Ref. [10]. In this case, a tubular geometry was chosen because of its simplicity and scalability. Each reactor body was made from a 2.54 cm copper tube (1″ nominal external diameter), 21 cm long. The reactor heads were made from VCO fittings, each adapted to include a welded stainless steel sintered filter (0.5 μm) and a tube fitting to secure the thermocouples. The reactors were horizontally arranged and filled with HFM to about half their volume in order to both reduce internal mechanical tensions due to the material compaction and to leave some extra free volume for the non-absorbable gaseous contaminants. Additionally, this arrangement prevents limitations with the permeability of the beds, as there is enough free space inside the reactors and the powder is loose.

In order to improve the internal thermal conductivity of the beds, 30 g of curled copper wires were included in each reactor. A schema of the reactors design is shown in Fig. 2. The reactors were thermally coupled by three 2 mm thick copper clamps and conductive silicon paste. This simple and robust solution greatly reduces the temperature variations in comparison to a non-coupled schema, as will be discussed below.

2.3. Hydride forming material

Each reactor was filled with 150 g of low cost, commercial purity $LaNi_5$ chunks (>97% purity, Whole Win (Beijing) Materials Sci. & Tech. Co., Ltd.). The characteristic thermodynamic parameters of this material were obtained via the vant'Hoff relation from volumetric measurements. The results are presented in Table 1. A surface fluorination treatment was applied to the material in order to facilitate its activation [11]. The treatment was performed by immersing 400 g of $LaNi_5$ in a solution of 4 cm^3 of hydrofluoric acid (50 wt%, density 1,16 g/cm^3) and 120 cm^3 of distilled water, for 30 min. Activation was achieved at room temperature under 900 kPa of pure H_2.

3. Model

A phenomenological model was developed in order to study and evaluate the prototype behavior in a wide range of conditions. This model would allow extrapolating the device response to working conditions not available at the laboratory scale and testing different scenarios without the need of performing multiple additional experiments. In order to model this system it is necessary to describe the thermodynamic behavior and the materials reaction kinetics.

The equilibrium pressure within the HFM miscibility gap (or plateau) can be described by the expression presented in Ref. [12] which has been used by numerous authors:

$$P_{pl} = P^0 \exp\left[-\frac{\Delta H}{RT} + \frac{\Delta S}{R} + f_s\left(\xi - \frac{1}{2}\right)\right] \quad (1)$$

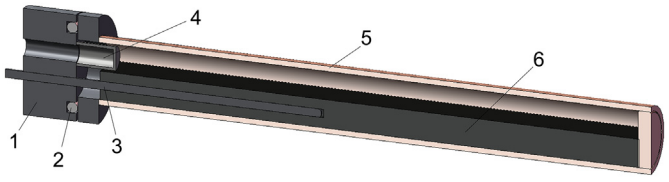

Fig. 2. Reactor design. 1: VCO reactor head. 2: O-Ring. 3: Thermocouple. 4: Stainless steel sintered filter. 5: Reactor body (copper). 6: Reaction bed ($LaNi_5$ + copper wires).

Table 1
Reaction enthalpy and entropy of the HFM.

ΔH_{abs} (kJ/mol)	ΔS_{abs} (J/mol K)	ΔH_{des} (kJ/mol)	ΔS_{des} (J/mol K)
−31.8 (2)	−112.0 (5)	32.7 (1)	113.0 (2)

Here, ξ is the reacted fraction (defined as the ratio of the actual and the maximum H concentration in the alloy), P^0 the reference pressure of 100 kPa and f_s is a slope coefficient. For the material used in this work, a value of $f_s = 0.26$ was measured. In order to describe the regions outside the plateau, we introduce *ad hoc* factors. The complete expression for the equilibrium pressure P_{eq} is as follows:

$$P_{eq} = \begin{cases} P_{pl}\left[1 - \frac{1}{2}\cos\left(\pi\frac{\xi}{\xi_\alpha}\right)\right] & \text{if } 0 < \xi < \xi_\alpha \\ P_{pl} & \text{if } \xi_\alpha < \xi < \xi_\beta \\ P_{pl} \Big/ \left[1 - \frac{1}{2}\cos\left(\pi\frac{1-\xi}{1-\xi_\alpha}\right)\right] & \text{if } \xi > \xi_\beta > 1 \end{cases} \quad (2)$$

Here, ξ_α and ξ_β are the values of the reacted fraction at the limits of the plateau and P_{pl} corresponds to Eq. (1), using the absorption or desorption thermodynamic parameters appropriately.

All absorption kinetics experimental results were reported in a previous paper [13]. To describe the reaction kinetics, rather than examining the details of the microscopic mechanisms involved [13], in this case an empirical global expression is proposed by separating variables. Under the present schema, the temperature dependence can be described by an Arrhenius equation that includes a kinetic coefficient k_0 and an effective value of the activation energy E_a^{eff} for the global process. The values found for these parameters are $k_0 = 500\ s^{-1}$ and $E_a^{eff} = 23.9$ kJ/mol. For the hydrogen concentration dependence, several possible reaction models were considered [14]. Among them, a 1st order Johnson-Mehl-Avrami (JMA) model was found to accurately describe our experimental results. Finally, within the range of conditions studied ($P < 1000$ kPa), a linear dependence with the external pressure was found to reproduce the results better than logarithmic dependences or other commonly used expressions [15]. The complete reaction kinetics description results as follows:

$$\frac{d\xi}{dt} = \begin{cases} k_0 exp\left[-\frac{E_a^{eff}}{RT}\right]\frac{|P - P_{eq}|}{P_{eq}}(1-\xi) & (abs.) \\ k_0 exp\left[-\frac{E_a^{eff}}{RT}\right]\frac{|P - P_{eq}|}{P_{eq}}\xi & (des.) \end{cases} \quad (3)$$

Eq. (2) and Eq. (3) are complemented with expressions for the gas state, heat generation, heat transfer and gas transport through valves, filters and mass flow controllers. The volume variation of the material due to the phase change has also been considered. Heat capacities of the different phases were taken from Ref. [16]. A summary of the parameters used is presented in Table 2.

4. Results

4.1. Model validation

A set of experiments using pure hydrogen was performed in order to validate the proposed model. In the first place, experiments consisting in filling up the empty reactors with hydrogen gas were performed in order to measure their internal volumes and to evaluate the loss factor due to the filters. After charging and activating the HFM in the reactors, several measurements were

Table 2
Summary of the parameters used in the simulation of the reference case.

Parameter	Value
Metal specific heat	0.351 J/g K ([16])
Hydride specific heat	0.547 J/g K ([16])
Metal density	8.310 g/cm^3 ([17])
Cell volume variation	21% ([18])
Capacity	1.35 wt%
Absorption enthalpy	−31.8 kJ/mol
Absorption entropy	−112 J/mol K
Desorption enthalpy	32.7 kJ/mol
Desorption entropy	113 J/mol K
Slope coefficient	0.26
Plateau start	0.1
Plateau end	0.9
Activation energy	23.9 kJ/mol
Kinetic coefficient	500 s^{-1}
Reactor 1 vol	72.4 cm^3
v_1 to filter 1 vol	21 cm^3
Reactor 2 vol	71.6 cm^3
v_2 to filter 2 vol	52 cm^3
F_i to v_1 volume	14 cm^3
Heat exchange surface	140 cm^2
Internal heat transfer	7.5 W/m^{2}K
External heat transfer	120 W/m^{2}K
Reactor body heat capacity	50 J/K
Intermediate heat capacity	200 J/K
Supply pressure	800 kPa
Room temperature	296 K

performed. They included constant flow charges and discharges of the reactors at different flow rates, both in the thermally coupled and isolated conditions. Macroscopic parameters related to the reactors, such as effective heat transfer surface areas and heat transfer coefficients were calculated from the results.

The results from selected experiments are shown in Fig. 3, together with the corresponding model predictions. For low gas flow values, the reaction takes place near equilibrium and the temperature distribution is approximately uniform. Fig. 3(a) and (b) show results and simulations of pressure and temperature evolutions, respectively, during a process of low constant flow charge of one reactor. The other reactor remains closed and is thermally coupled with the first one. In this condition the model results closely match those from the experiments. The same type of experiments was performed at higher flow values (Fig. 3(c) and (d)). In these cases, the lumped model approximation is less accurate and the results show some discrepancy, but still remain within satisfactory margins.

Fig. 3(e) and (f) show results from the first few cycles of a purification process as described in Section 2.1, using pure hydrogen as feed gas, with the reactors working in opposition. Only results from one of the reactors are shown, which is initially in desorption stage. Variations of room temperature are not accounted for in the simulations. The model results are again satisfactory.

Here, due to the thermal coupling schema, the heat generated in the absorption reaction at one reactor is mostly used by the desorption reaction, reducing temperature variations in both

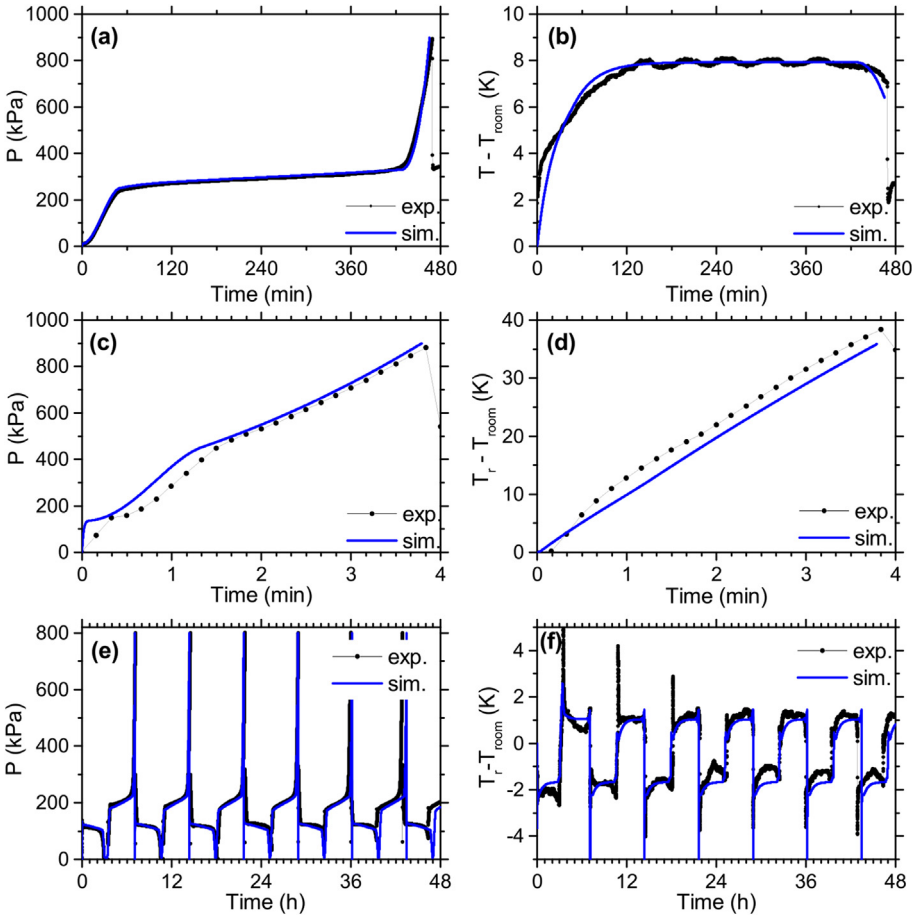

Fig. 3. Experimental and simulated results under selected conditions using pure hydrogen. **(a,b)** Single charge at 50 sccm. **(b,c)** Single charge at 2000 sccm. **(e,f)** Cyclic process at 100 sccm.

reaction beds. This effect is apparent when comparing the temperature evolution during a single charge of one reactor with a cyclic coupled process. For example, at 50 sccm, the temperature raises about 8 K during a single charge, as it can be seen in Fig. 3(b). If a desorption experiment is carried out in the same conditions, the temperature drops by about the same value. Therefore, if the reactors were not coupled, the temperature difference should be of about 16 K. However, when a coupled cyclic process at 100 sccm is implemented as in Fig. 3(f), the temperature difference is reduced to less than 3 K, even though the generated heat rate roughly doubles that of the former case.

4.2. Process performance

The recovered fraction, defined as the ratio between the total hydrogen output and the total gas input, was chosen as a measure of the performance of the process. This ratio was calculated by simulating 100 complete cycles and averaging the recovered fraction from cycles 80 to 100. In this way, all transient effects are eliminated from the calculations, yielding stationary regime results. This magnitude was calculated as a function of the gas flow under different scenarios, as shown in Fig. 4(a). This curve shows a high recovery region for lower flow rates, reaching hydrogen recovery fractions over 97%. These high recovered fractions are maintained up to a critical point (crisis) at about 800 standard cm^3/min (sccm), where it starts diminishing. This crisis, marked with an upwards arrow in the figure, corresponds to the flow value where the desorption kinetics is not fast enough for the hydride to fully decompose before starting a new cycle, as it can be seen in Fig. 4(b) and (c). These two figures show the evolution of the reacted fraction vs. time during cyclic processes at 200 sccm and 1000 sccm, respectively (marked as **B** and **C**, respectively, in Fig. 4(a)). The first value is well below the desorption critical point, whereas the second is over it. The figure shows that for the lower flow value, both absorption and desorption reactions develop almost completely, spanning the entire plateau. In contrast, for the higher flow value the desorption phase is not complete and only a fraction of the material's storage capacity is effectively used, lowering the recoverable amount of pure hydrogen. At about 7000 sccm, a second critical point is apparent (marked with a downwards arrow in Fig. 4(a)), which corresponds to a similar crisis related to the absorption process.

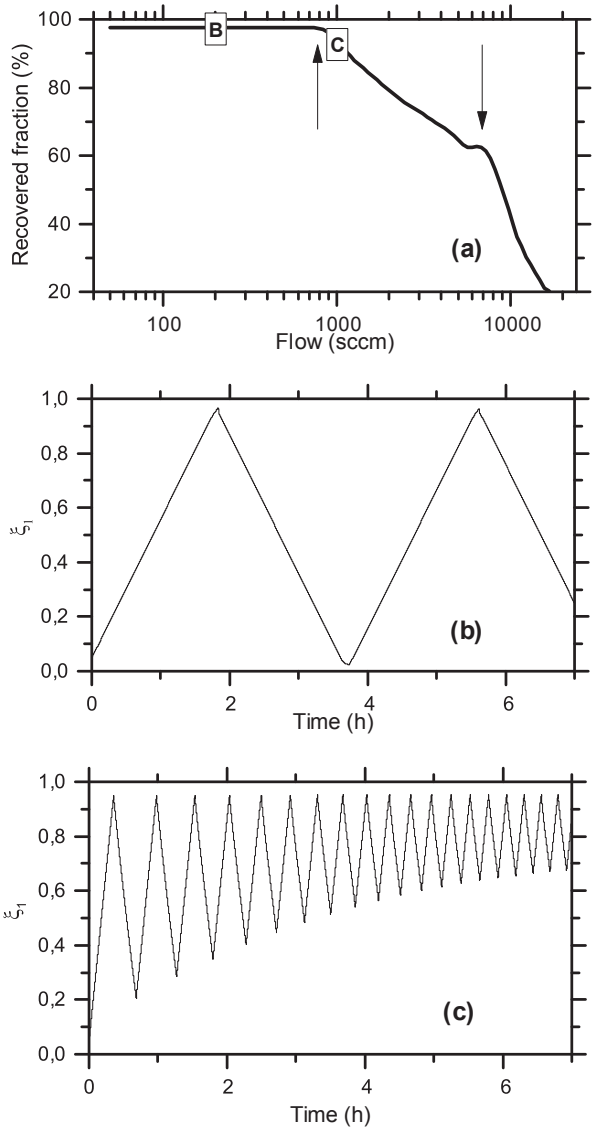

Fig. 4. **(a)** Hydrogen recovered fraction vs. gas flow. Arrows mark the critical points. **(b,c)** Reacted fraction vs. time at points **B** and **C**, respectively, as marked in **(a)**.

The positions of these two crises are defined by both the intrinsic reaction kinetics and the conditions set for each case. Results corresponding to the actual experimental conditions (Fig. 4(a)) are included in all graphs as a reference case (see curve marked as “ref.” in Fig. 5 a–f). In this reference case, absorption conditions are more favorable than desorption conditions and thus, the desorption critical flow is lower than the absorption critical flow. In Fig. 5(a) the hydrogen recovery curve is reproduced for different values of the supply pressure. As this pressure diminishes, the absorption critical flow lowers, while the desorption conditions remain unchanged. In one case, with the lower supply pressure, the absorption critical flow is even lower than the desorption critical flow. It should also be noted that when the supply pressure is higher, the amount of hydrogen in the gas phase at the end of the absorption stage is also higher, while the hydrogen contained in the solid hydride is roughly the same. As a result, more hydrogen is vented each cycle and the recovered fraction within the high recovery region is a little lower, as it is apparent in Fig. 5(a).

A different case can be seen in Fig. 5(b), which shows results of simulations performed with and without filter at the reactors inlets. The difference between the curves displays the effect of the pressure loss in the filter. This loss retards both absorption and desorption reactions, shifting the corresponding critical values to lower flow regions. Regarding the recovered fraction for lower flow values, the difference is more important than in the previous case. During the venting stage, the gas present in the reactor is evacuated abruptly, at a very high flow rate, for a few seconds. The filter presents a restriction to this gas flow, which is therefore higher without filter than with filter. As a result, more hydrogen is lost during the venting stage when the filter is not present and therefore the recovered fraction is lower in this case. This effect could be compensated by diminishing the venting time, but this optimization was not performed for this analysis.

The chosen schema assumes that both reactors are thermally coupled through an intermediate mass, which in turn dissipates heat to the environment. Thus, two heat transfer coefficients exist: U_{ri}, between the bed and the intermediate mass, and U_{ia}, between this mass and the room. Fig. 5(c) shows the effect of changes in the heat transfer coefficients upon the hydrogen recovered fraction. Increasing U_{ri} four times over the reference situation increases the critical flow from 800 sccm to 1000 sccm, while decreasing it by the same factor reduces this value from 800 sccm to 400 sccm. This result indicates that the internal heat transfer is important for the

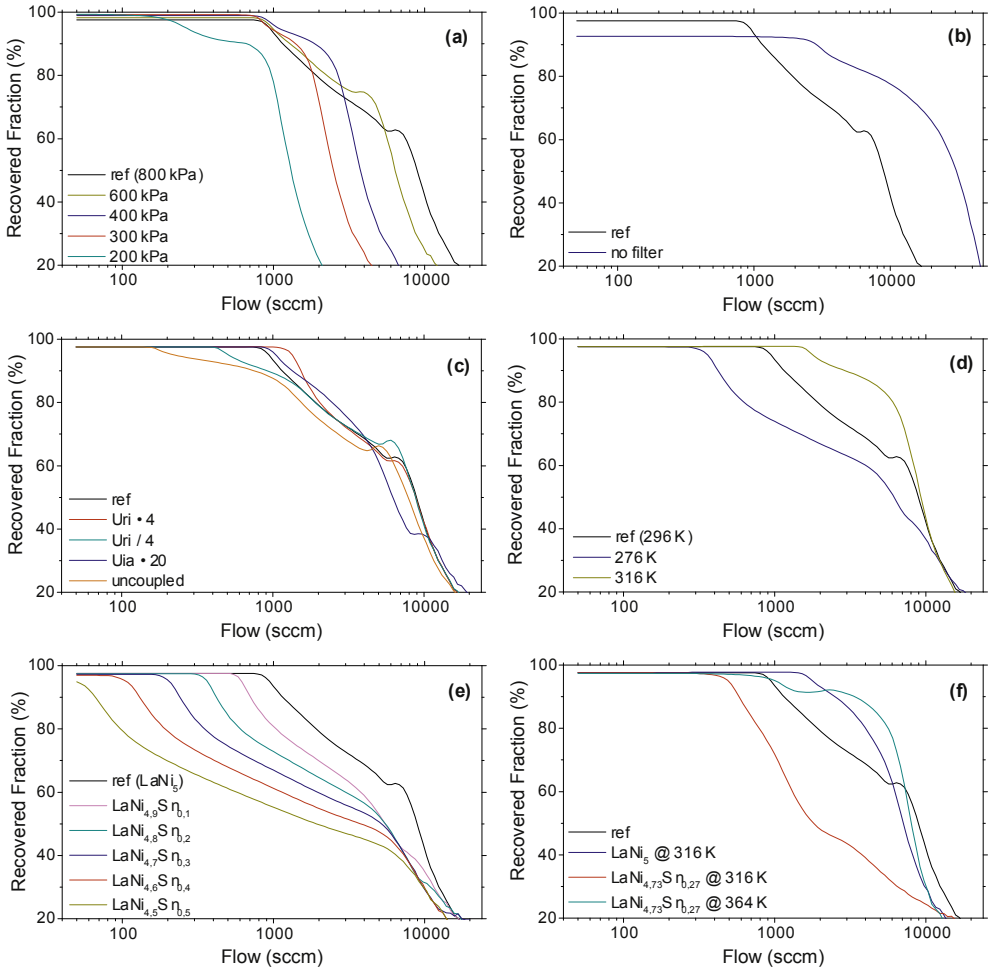

Fig. 5. Hydrogen recovered fraction vs. gas flow. Curves show the effect of: **(a)** Supply pressure. **(b)** Filter pressure loss. **(c)** Heat transfer configurations. **(d)** Temperature. **(e)** Alloy composition. **(f)** CO contamination (10 ppm)/Alloy composition and temperature. The same reference condition from Fig. 4(a) is included in all graphs.

efficiency of the whole system. Considering the heat transfer with the exterior, a previous report informs that for a similar setup the action of circulating water around the reactor increases U_{ia} by a factor of 20 [19]. Nevertheless, as it can be seen in Fig. 5(c), the effect of this improvement does not play an important role under the present scenario. These results indicate that, for the coupled reactors setup, improving the internal heat transfer is more effective than improving the heat exchange with the surrounding ambient for achieving high amounts of hydrogen recovery. The main reason behind this finding is the management of heat established by the reactors thermal coupling that takes advantage of the internal heat generated and consumed during hydride formation and decomposition reactions, respectively. Also included in Fig. 5(c) there is the corresponding curve for the thermally uncoupled scenario, in which each reactor only exchanges heat directly with the environment. In this case, the critical flow is reduced to 140 sccm, emphasizing the effect of the coupling schema proposed.

Fig. 5(d) shows the effect of the external temperature around the reactors on the overall process. It must be stressed that this temperature is, in general, not coincident with the actual reactors' temperatures due to the heat produced/consumed during hydride formation/decomposition reactions that take place in each cycle. In this sense, the external temperature simulates the presence of a thermal bath where the reactors could be embedded. For a higher temperature, the plateau pressure of the HFM increases, favoring the desorption reaction. Under a higher external temperature condition, the desorption critical flow increases with respect to the reference case. The opposite occurs when the temperature is lowered. Similar effects are found varying the material composition, which has been evaluated for various $LaNi_{5-x}Sn_x$ alloys (Fig. 5(e)). In this alloy family, increments in Sn content result in lower plateau pressures and smaller plateau spans [20]. The main result is, again, a shift of the desorption crisis to lower flow values, while the absorption critical flow is less affected.

Finally, as the main application of the device would be in hydrogen purification processes, it results of interest to analyze the effect of CO contamination over hydrogen recovery. These effects were evaluated for the conditions described in Ref. [21], where the authors found that CO strongly retards the reaction kinetics without affecting the total absorption capacity. As no established poisoning model is available, the global alloy behavior was modeled by modifying the kinetic constant in order to reproduce each scenario. The results are presented in Fig. 5(f) in terms of temperature and/or alloy modifications. For the case of $LaNi_5$ as HFM, the presence of 10 ppm of CO in the incoming gas stream can be compensated by an increase of 20 K in the external temperature as the desorption crisis occurs practically at the same flow value found for the reference case (without CO). In the case of the Sn substituted alloy at the same temperature the desorption crisis is

affected by alloy composition, as it was already discussed. Thus, an additional temperature increase would be necessary in order to obtain recovery and critical flow values comparable to the reference case.

4.3. Humidity removal

As a test case scenario, purification experiments using humidified hydrogen were performed. The choice of water vapor as contaminant relates to three key aspects: a) water vapor content is commonly monitored to determine the gas quality in industrial plants; b) water vapor content can be measured in-line; and c) the HFM purification method has been considered more suitable for less reactive impurities, making water vapor removal a particularly challenging scenario. The experiments were performed using $LaNi_5$ as HFM and a hydrogen flow of 100 sccm, where the water vapor content in the feed gas reaches a dew point of 12 °C at 370 kPa. Fig. 6 presents the main experimental results for one purification cycle using one reactor only.

Fig. 6(a) shows the pressure evolution. Initially, it rapidly increases up to the point where the hydride forming reaction occurs. When the HFM is completely hydrided the pressure starts to rapidly increase again. The absorption stage finishes when the reactor reaches the supply pressure. Then, a brief venting stage is seen as a sharp decrease in the pressure followed by the hydrogen desorption stage. This stage ends when all the stored hydrogen has been removed from the reactor. The simulated curve, also included in Fig. 6(a), closely follows the experimental results, although a small difference is apparent. Considering that the model was able to precisely reproduce the experimental results in the case of pure hydrogen (Fig. 6(a)), the difference found in this case can be attributed to the effect of humidity on the reaction kinetics, which has not been accounted for in the simulation.

The measured humidity content of the gas flow at the reactor inlet is presented in Fig. 6(b). The reactor pressure at the beginning of the cycle is very low and thus, the gas expands immediately after the flow controller. Due to this gas expansion, the dew point is lower than the value in the feed gas. As the experiment proceeds, the humidity content in the reactor increases up to the value of the feed gas (12 °C dew point). The humidity increase is also reflected in Fig. 6(c) and (d), which show the evolution of H_2O partial pressure and H_2O volumetric content during the cycle, respectively. The humidity sharply decreases when the system is vented down to a dew point value of around −30 °C, evidencing that most of the water vapor present in the system is eliminated at this stage. During the hydrogen desorption stage, the humidity lowers further as the remaining water vapor is swept by the hydrogen flow. The H_2O volumetric content has been calculated as the ratio between the H_2O partial pressure and the total reactor pressure. It should be mentioned that during the venting stage and at the end of the desorption stage the total pressure reaches very small values. At these points, the volumetric content quotient does not reflect a meaningful magnitude.

Considering the results from the process performance point of view, the humidity content was successfully lowered from 3800 ppm to 190 ppm, while reaching a hydrogen recovery fraction of 93%. This recovery value is slightly lower than the one predicted by the simulations of Section 4.2 because the venting time was increased from 5 s to 20 s in order to account for the humidity removal kinetics.

Fig. 7 shows results from a cyclic process under similar experimental conditions as those described for the case presented in Fig. 6. In order to maintain a reliable feed flow, the supply pressure was increased to 400 kPa, while the maximum pressure was kept at 370 kPa. As a result, the maximum dew point at the end of the absorption stage does not match that of the feed gas (12 °C), reaching a maximum value of about 8 °C. We also note that room temperature variations are not accounted for in the simulations. This results in some differences between the simulated and the experimental results, most notably around the fifth cycle shown. As it was mentioned for the previous case, the simulated results slightly overestimate the time required for each cycle, but otherwise reproduce well the experimental results.

During the cyclic process, the humidity content is lowered from

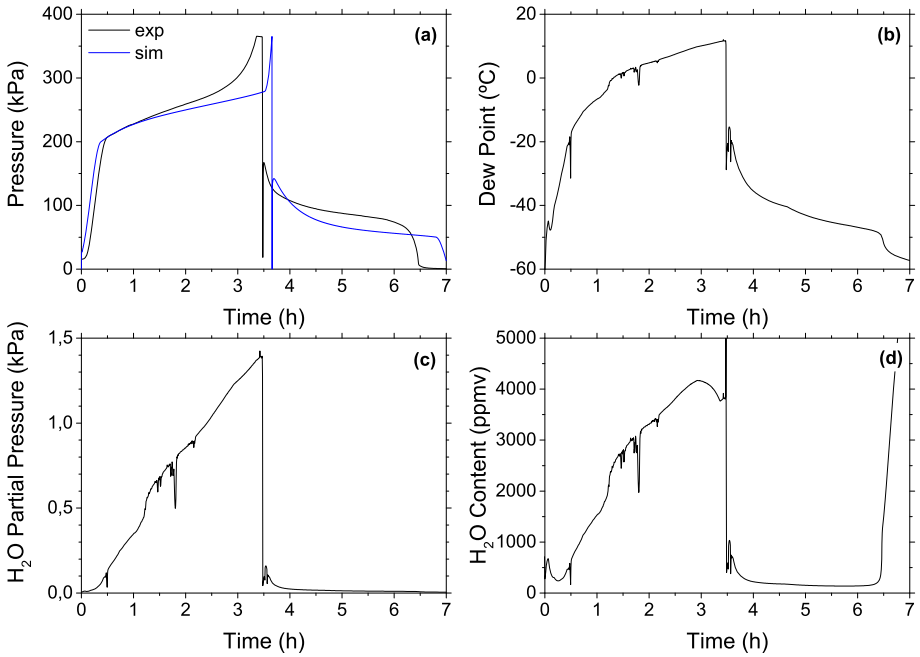

Fig. 6. Complete cycle using one reactor to purify humidified hydrogen. **(a)** Total pressure. **(b)** Dew point (experiment). **(c)** Water vapor partial pressure (experiment). **(d)** Volumetric water vapor content (experiment).

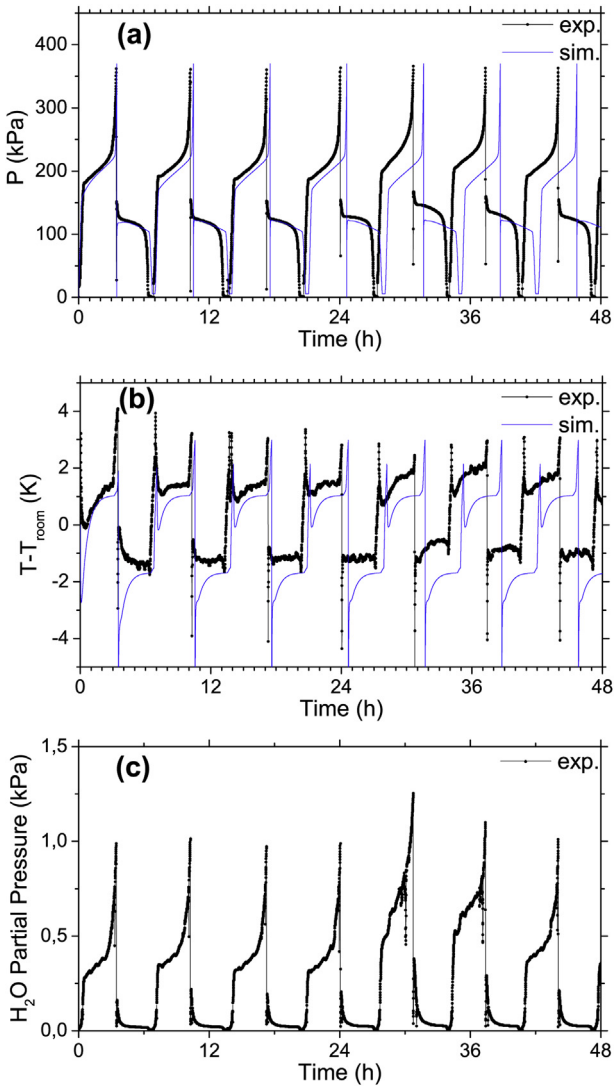

Fig. 7. Experimental and simulated results of a cyclic purification process at 100 sccm using humid hydrogen.

about 3000 ppmv to about the same value found before, of 190 ppmv. This suggests that the remnant humidity value does not vary strongly with the inlet dew point, and therefore the purification factor can be expected to be lower for less humid conditions. At the same time, the recovery fraction measured is slightly higher than the one obtained for the isolated cycle, presenting a value of 95%. While this fact could be related to the slightly lower dew point in the feed gas, it should be noted that for the isolated cycle experiment, a small variation in the initial hydrogen content in the HFM affects the recovery fraction obtained. Therefore, the value obtained over several cycles is more reliable.

The results shown in Fig. 7 are a fragment of a longer experiment. After 30 cycles of continuous operation, no significant degradation of the reaction properties has been found. The time required by each cycle presents variations of about 2%, depending on the room temperature, and it shows no significant trend with the cycle number. The amount of remnant humidity, as measured at the end of each desorption stage, presents a similar behavior, indicating that no significant water accumulation occurs. A long-term study of the system behavior will be reported in a future work.

5. Conclusions

A hydrogen purification system has been designed where two thermally coupled reactors containing 300 g of $LaNi_5$ mixed with Cu wires work in opposition without heat sources or sinks. The system has been built and characterized. A phenomenological model describing the system operation has been proposed and validated. The model was used to test the influence of several factors such as the feed flow, supply pressure, external temperature, alloy composition, heat exchange configurations and CO impurity presence in the feed gas. The simulations show that the system can provide a hydrogen recovery fraction over 97% working at room temperature and feed flows up to 800 sccm. The system performance has been experimentally tested using humidified hydrogen. The device successfully lowered the humidity content from 3000 ppm to 190 ppm of an incoming flow of 100 sccm at room temperature, while reaching a hydrogen recovery fraction of 95%. The process behavior has been verified during 30 cycles of continuous operation in humid hydrogen, after which no degradation has been found. The obtained results open up the possibility of using this hydrogen purification strategy for small- and medium-scale industrial applications.

Acknowledgements

The authors thank ANPCyT (PICT 2012-1796) and U.N. Cuyo (Research Project 06/C417) for the financial support. The reactors were built with the help of Mr. F. Roldán and Mr. N. Aversente. Ing. E. Neuman contributed with helpful discussions.

References

[1] M.M.H. Bhuiya, A. Kumar, K.J. Kim, Metal hydrides in engineering systems, processes, and devices: a review of non-storage applications, Int. J. Hydrogen Energy 40 (2015) 2231–2247, http://dx.doi.org/10.1016/j.ijhydene.2014.12.009.

[2] X.Y. Chen, L.X. Wei, L. Deng, F.S. Yang, Z.X. Zhang, A review on the metal hydride based hydrogen purification and separation technology, Appl. Mech. Mater. 448–453 (2014) 3027–3036, http://dx.doi.org/10.4028/. www.scientific.net/AMM.448-453.3027.

[3] V.I. Artemov, K.B. Minko, G.G. Yan, Numerical study of heat and mass transfer processes in a metal hydride reactor for hydrogen purification, Int. J. Hydrogen Energy 41 (2016) 1–7, http://dx.doi.org/10.1016/j.ijhydene.2016.01.124.

[4] J.J. Sheridan, F.G. Eisenberg, E.J. Greskovich, G.D. Sandrock, E.L. Huston, Hydrogen separation from mixed gas streams using reversible metal hydrides, J. Less Common Mater. 89 (1983) 447–455, http://dx.doi.org/10.1016/0022-5088(83)90355-7.

[5] F. Block, A. Dey, H. Kapes, K. Reith, Hydrogen purification with metal hydrides in a new kind of reactor, J. Less Common Met. 131 (1987) 329–335, http://dx.doi.org/10.1016/0022-5088(87)90532-7.

[6] M. Au, C. Chen, Z. Ye, T. Fang, J. Wu, O. Wang, The recovery, purification, storage and transport of hydrogen separated from industrial purge gas by means of mobile hydride containers, Int. J. Hydrogen Energy 21 (1996) 33–37, http://dx.doi.org/10.1016/0360-3199(95)00044-E.

[7] S. Miura, A. Fujisawa, M. Ishida, A hydrogen purification and storage system using metal hydride, Int. J. Hydrogen Energy 37 (2012) 2794–2799, http://dx.doi.org/10.1016/j.ijhydene.2011.03.150.

[8] M. Lototskyy, K.D. Modibane, M. Williams, Y. Klochko, V. Linkov, B.G. Pollet, Application of surface-modified metal hydrides for hydrogen separation from gas mixtures containing carbon dioxide and monoxide, J. Alloys. Compd. 580 (2013) S382–S385, http://dx.doi.org/10.1016/j.jallcom.2013.02.096.

[9] B.A. Talagañis, G.O. Meyer, D.G. Oliva, M. Fuentes, P.A. Aguirre, Modeling and optimal design of cyclic processes for hydrogen purification using hydride-forming metals, Int. J. Hydrogen Energy 39 (2014) 18997–19008, http://dx.doi.org/10.1016/j.ijhydene.2014.09.045.

[10] X.L. Wang, S. Suda, Surface characteristics of fluorinated hydriding alloys, J. Alloys. Compd. 231 (1995) 380–386, http://dx.doi.org/10.1016/0925-8388(95)01851-4.

[11] F.S. Yang, G.X. Wang, Z.X. Zhang, X.Y. Meng, V. Rudolph, Design of the metal hydride reactors - a review on the key technical issues, Int. J. Hydrogen Energy 35 (2010) 3832–3840, http://dx.doi.org/10.1016/j.ijhydene.2010.01.053.

[12] Z. Zhou, J. Zhang, J. Ge, F. Feng, Mathematical modeling of the PCT curve of hydrogen storage alloys, Int. J. Hydrogen Energy 19 (1994) 269–273, http://dx.doi.org/10.1016/0360-3199(94)90097-3.

[13] M.V. Blanco, E.M. Borzone, A. Baruj, G.O. Meyer, Hydrogen sorption kinetics of La-Ni-Sn storage alloys, Int. J. Hydrogen Energy 39 (2014) 5858–5867, http://dx.doi.org/10.1016/j.ijhydene.2014.01.125.
[14] A. Khawam, D.R. Flanagan, Solid-state kinetic models: basics and mathematical fundamentals, J. Phys. Chem. B 110 (2006) 17315–17328, http://dx.doi.org/10.1021/jp062746a.
[15] M. Ron, The normalized pressure dependence method for the evaluation of kinetic rates of metal hydride formation/decomposition, J. Alloys. Compd. 283 (1999) 178–191, http://dx.doi.org/10.1016/S0925-8388(98)00859-7.
[16] D. Ohlendorf, H.E. Flotow, Experimental heat capacities of $LaNi_5$, α-$LaNi_5H_{0.36}$, and β-$LaNi_5H_{6.39}$ from 5 to 300 °K. Thermodynamic properties of the $LaNi_5$–H_2 system, J. Chem. Phys. 73 (1980) 2937, http://dx.doi.org/10.1063/1.440467.
[17] J.-M. Joubert, R. Černý, M. Latroche, E. Leroy, L. Guénée, A. Percheron-Guégan, K. Yvon, A structural study of the homogeneity domain of $LaNi_5$, J. Solid State Chem. 166 (2002) 1–6, http://dx.doi.org/10.1006/jssc.2001.9499.
[18] M. Stange, J.P. Maehlen, V.A. Yartys, P. Norby, W. Van Beek, H. Emerich, In situ SR-XRD studies of hydrogen absorption-desorption in $LaNi_{4.7}Sn_{0.3}$, J. Alloys. Compd. 404–406 (2005) 604–608, http://dx.doi.org/10.1016/j.jallcom.2005.01.124.
[19] Y. Kaplan, Effect of design parameters on enhancement of hydrogen charging in metal hydride reactors, Int. J. Hydrogen Energy 34 (2009) 2288–2294, http://dx.doi.org/10.1016/j.ijhydene.2008.12.096.
[20] E.M. Borzone, A. Baruj, M.V. Blanco, G.O. Meyer, Dynamic measurements of hydrogen reaction with $LaNi_{5-x}Sn_x$ alloys, Int. J. Hydrogen Energy 38 (2013) 7335–7343, http://dx.doi.org/10.1016/j.ijhydene.2013.04.035.
[21] E.M. Borzone, M.V. Blanco, G.O. Meyer, A. Baruj, Cycling performance and hydriding kinetics of $LaNi_5$ and $LaNi_{4.73}Sn_{0.27}$ alloys in the presence of CO, Int. J. Hydrogen Energy 39 (2014) 10517–10524, http://dx.doi.org/10.1016/j.ijhydene.2014.05.004.